42nd AIAA/ASME/SAE/ASEE Joint Propulsion Conference and Exhibit
Sacramento, California
9-12 July 2006

Towards the Identification of the Keeper Erosion Cause(s): Numerical Simulations of the Plasma and Neutral Gas Using the Global Cathode Model OrCa2D-II.

Ioannis G. Mikellides,[*] Ira Katz,[†] Dan M. Goebel,[‡] and Kristina K. Jameson[§]
Jet Propulsion Laboratory, California Institute of Technology, Pasadena, CA, 91109

Numerical simulations with the time-dependent Orificed Cathode (OrCa2D-II) computer code show that classical enhancements of the plasma resistivity can not account for the elevated electron temperatures and steep plasma potential gradients measured in the plume of a 25-27.5 A discharge hollow cathode. The cathode, which employs a 0.11-in diameter orifice, was operated at 5.5 sccm without an applied magnetic field using two different anode geometries. It is found that anomalous resistivity based on electron-driven instabilities improves the comparison between theory and experiment. It is also estimated that other effects such as the Hall-effect from the self-induced magnetic field, not presently included in OrCa2D-II, may contribute to the constriction of the current density streamlines thus explaining the higher plasma densities observed along the centerline.

I. Introduction

A detailed modeling effort, supported by a rigorous experimental investigation, was initiated in 2004 at JPL to assess the life of orificed hollow cathodes for electric propulsion. The goal of the modeling effort has been to generate a global orificed cathode model that can predict accurately the evolution of the plasma in all regions of the cathode. The model could then be used to predict the life of the cathode and offer mitigating designs if needed. The inherent two-dimensionality of the plasma both inside and outside the orificed cathode leaves (at best) little hope that 0D and 1D theoretical models can provide the understanding necessary for the identification, quantification and mitigation of the mechanisms that determine cathode life. Inside the cathode, 2D models that do not account for the coupling that exists between the plasma and the emission characteristics along the insert boundary, assume uniform electron temperature, and/or do not account for all the dominant particle collision physics (such as ion-neutral collisions) are also insufficient in determining the extent to which the emitter is utilized, and ultimately its life. Based on recent modeling by Mikellides *et al.*,[1] the physical processes that occur inside the orifice channel and conical regions strongly influence the way the plasma evolves in the near-plume region. Thus, de-coupling the two regions to simulate the plume separately would automatically force a dependence of the solution on the assumed boundary conditions, and as a consequence, the sensitivity of the solution on the choice of boundary conditions would be in question. The possible existence of non-classical heating in the orifice and near-plume regions also require that the appropriate terms representing these physics appear in the conservation laws which may include anomalous resistivity and time-dependence. Also, the long thermal equilibration times between electrons and ions imply that ions remain cold relative to the electrons in the near-plume region which means that a separate energy equation must be solved for the heavy species. Capturing the electron-to-ion temperature ratio (T_e/T_i) is critical because it strongly determines the level of damping one would expect in many mechanisms that promote wave growth. The Orifice Cathode (OrCa2D-II) computer code has been under development at JPL since 2005 as a global,

[*] Member Technical Staff, Advanced Propulsion Technology Group, 4800 Oak Grove Drive, Pasadena, CA, 91109, Mail Stop 125-109, Senior Member AIAA.
[†] Group Supervisor, Advanced Propulsion Technology Group, 4800 Oak Grove Drive, Pasadena, CA, 91109, Mail Stop 125-109, Senior Member AIAA.
[‡] Section Staff, Thermal and Propulsion Engineering Section, 4800 Oak Grove Drive, Pasadena, CA, 91109, Mail Stop 125-109, Senior Member AIAA.
[§] Academic Part Time Staff, Thermal and Propulsion Engineering Section, 4800 Oak Grove Drive, Pasadena, CA, 91109, Mail Stop 125-109, Member AIAA.

rigorous theoretical model of the hollow cathode that includes both the emitter and plume regions. We report here on several new findings from simulations of the 1.5-cm high-current hollow cathode.

II. Theoretical Model

A. General Description

The governing conservation laws and numerical approach for the OrCa2D-I & II codes have been presented in detail in previous publications[1,2] and will not be repeated here. In summary, the coupled system consists of eight governing laws for the plasma and neutral gas and yields the steady-state profiles of the following (main) variables: plasma particle density n, ion and electron current densities $\mathbf{j}_i$ and $\mathbf{j}_e$, electron temperature T_e, electric field $\mathbf{E}$, plasma potential ϕ, neutral particle density n_n and heavy species temperature T. The system includes two energy equations and non-equilibrium ionization. The inertia terms are neglected in both the electron and ion momentum equations. Functional forms of the collision frequencies have also been provided in Ref **Error! Bookmark not defined.**. It is assumed that ions and neutrals are in thermal equilibrium so a single equation is derived for the conservation of energy of the heavy species. OrCa2D-II solves one additional conservation law, namely the neutral gas momentum equation, which yields the neutral gas flux $\mathbf{\Gamma}_n$. Sheath funneling and emission turnoff boundary conditions along the emitter were shown to be negligible for the larger cathode simulated here and have therefore been neglected.[Error! Bookmark not defined.] The region of space simulated by OrCa2D-II is illustrated in (FIG?).

The conservation equations are descretized using finite volumes with all vectors defined at cell edges and all scalars defined at cell centers. The system is solved in a time-split manner with the plasma equations heavily implicitized. The neutral gas continuity and momentum equations are solved explicitly. The numerical approach for the neutral gas momentum equation uses an upwind finite volume scheme by applying the Godunov 1st-order upwind fluxes across each edge in the same way it is done for one-dimensional problems. No flux-limiting is presently employed.

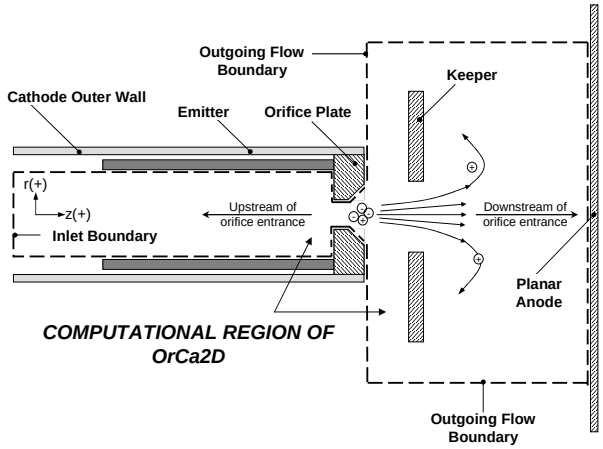

Fig 1. Schematic of the hollow cathode emitter, orifice and plume regions showing the OrCa2D computational region (dashed line).

B. Code Improvements

As indicated in the introduction, several code improvements were shown necessary by previous work before OrCa2D-II may be used routinely to assess keeper erosion of different-size cathodes at various operating conditions: (1) incorporate keeper electrode boundary in the simulated geometry, (2) incorporate neutral gas collisional-to-rarefied transition physics, (3) improve computational speed. All have been accomplished this year and are briefly described in this section.

1. Computational Grid

Previous work with OrCa2D-II utilized a rectilinear grid which simplified the numerical descritization of the governing equations but introduced errors in the far plume regions largely because the grid cells became highly non-conformal in those regions. To reduce such errors more grid cells had to be incorporated which led to exceedingly long computational times. Typical execution times with the rectilinear version of OrCa2D-II FIG? (top) were in the order of a few weeks. The new computational grid constructed is shown in FIG? (bottom). It uses mixed rectilinear and non-rectilinear quadrilateral cells to retain descritization simplicity wherever possible, while reducing the

number of cells in the plume region by going to generalized-geometry quadrilaterals that retain good orthogonal and conformal properties where resolution is needed the most (i.e. in the near plume region). With new grid the computational times have been reduced by more that one order of magnitude. The keeper electrode has also been incorporated in the new geometry. The gap between the orifice plate and keeper is not included in any of the simulations. It is assumed that the keeper inner wall extends up to the orifice plate exit.

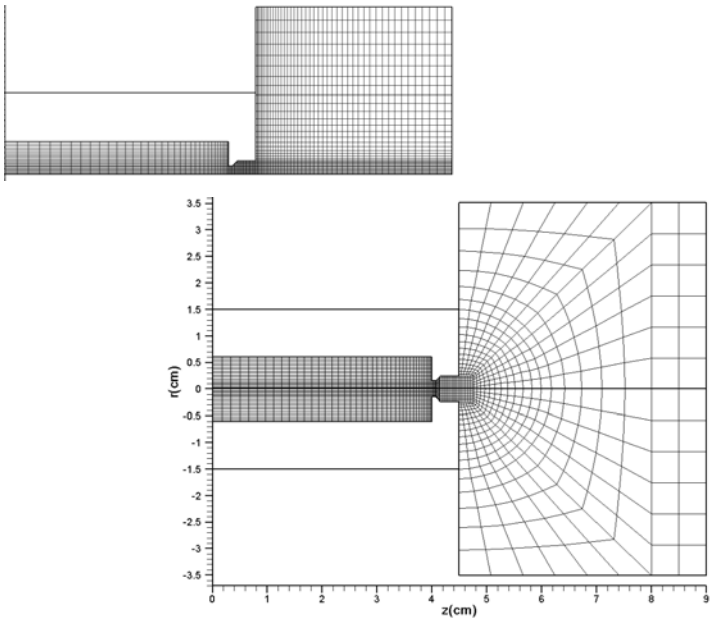

Fig 2. Top: Original rectilinear grid (2723 cells). Bottom: New mixed rectilinear-curvilinear grid (1092 cells).

2. Neutral Gas Model

The simulations with OrCa2D-II up to this point have assumed that the continuum approximation is valid for the neutral gas throughout the computational region. However, for the simulated cathode studied here the mean free paths for neutral collisions become comparable to the characteristic dimensions inside the orifice and can be many times the keeper diameter in the keeper region as shown in FIG? (top right). The continuum solution predicts the existence of stationary compression waves (see FIG? right-bottom) as the sonic flow exiting the orifice entrance expands to supersonic speeds through a Prandtl-Meyer expansion fan and impinges on the keeper inner walls. In reality however, the steep gradients associated with these waves can not be supported by the rarefied gas as a consequence of the loss of collisionality between particles.

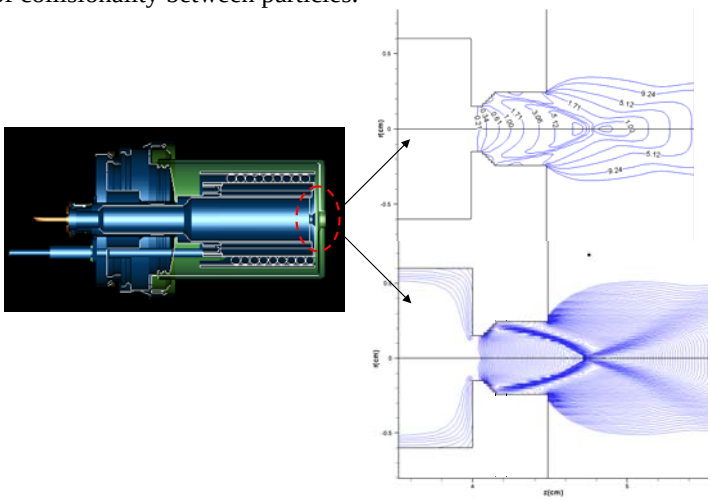

Fig 3. Neutral gas density mean free paths and density contours computed using full fluid approach.

For the simulation of the rarefied regions it is customary to implement particle methods such as Direct Monte Carlo Simulation or Particle-in-Cell. A few facts, that are specific to the hollow cathode problem, make particle methods unfavorable. First, the inherent statistical fluctuations associated with particle methods introduce numerical noise which would make the interpretation of the real oscillations observed in the plasma (FIG? REF HERE Goebel IEPC) difficult. Second, in the highly collisional region of the high-current (>25 A) cathodes studies here particle methods would require exceedingly many particles and consequently impractical computational times. A combined fluid-particle approach would be most fitting but the coupling of the two regions and the associated boundary conditions are still an active area of research.

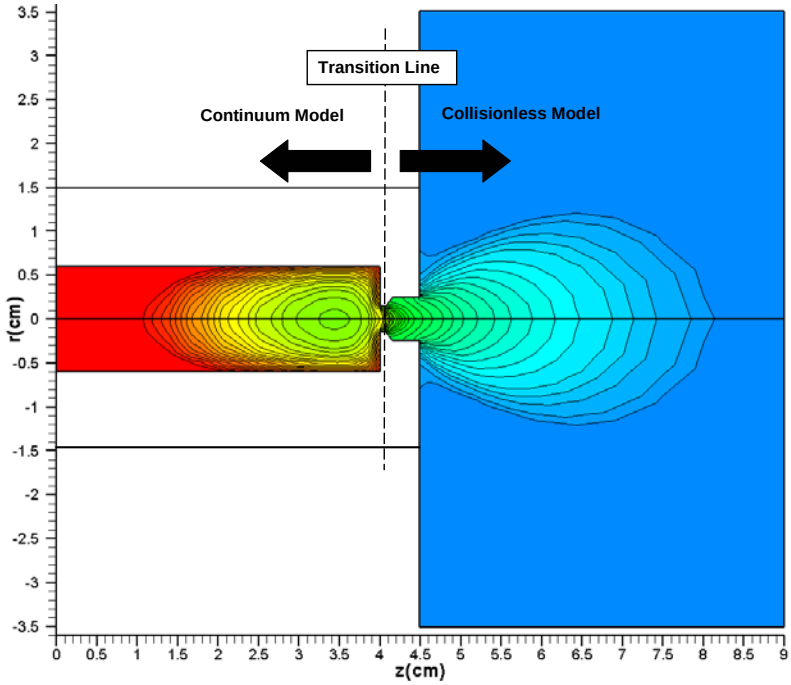

Fig 4. Fig 4. Neutral gas density contours computed using the new fluid-collisionless approach.

Due the large system of equations that must be solved in the hollow cathode, as rendered by the strong coupling between the neutral gas and the plasma, computationally-cheap approaches must be devised which sacrifice some accuracy for the sake of computational speed and smoothness of the solution. Here, we take advantage of the low degree of ionization in the plume (~5%) to assume that the gas particles expand freely in straight line trajectories from a pre-defined boundary chosen in the present simulations to be the orifice exit. The basic principle is that the gas emanates from a surface with a positive normal velocity and a thermal spread perpendicular to that surface. Then at large distances from the surface the perpendicular velocity spread is reduced due to geometrical selection. The purely collisionless flux of particles is thus only altered by either an ionization event or an encounter with walls. To account for the first, the continuity equation for the neutrals (EQNFIG? below)

$$\frac{dn_c^k}{dt} = \sum_{j=1}^{4}\left(n_{cj}^k u_k^+ - n_c^k u_k^-\right)\Delta S_j - n_c^k\left(n_e \sigma_{iz}\, u_{T,e}\right)\Delta V_c \rightarrow n_c = \sum_{k=1}^{N} n_c^k \qquad (1)$$

retains the ionization term which allows for the loss of neutral particles in consistence with the plasma continuity equations. For the second, particles impacting the walls are assumed to undergo specular reflection and return back into the computational region with the thermal speeds that are determined based on the local wall temperature. Under these assumptions the problem then becomes one of computing all the geometrical view factors (but only once) and keeping track of particle fluxes associated with the various wall boundaries. To compute the view factors all surfaces are triangulated in three dimensions. There are k=6 different wall boundary temperatures and therefore

six continuity equations must be solved for the neutrals. It is noted that each continuity equations must account for the flux of all "types" of particles crossing each edge of a computational cell. The approach is described with greater detail in FIG? REF IRA's 2006 JPC PAPER. FIG? shows the solution for a typical NEXIS cathode operating condition (5.5 sccm, 25 A). The particular solution shown below used a plasma solution that has been frozen in time. The continuum region is still modeled using the previous fluid approach. The two regions are coupled at the transition line by assuming that no particles from the collisionless region enter the continuum region, which is a good approximation since the flux of neutrals from the continuum region is the dominant flux at the transition line. Then the transition line simply becomes another "emission" surface for the collisionless region at the local gas temperature, which is determined by solving the combined ion-neutral (or heavy-species) energy equation. Beyond the transition line the terms in the energy equation associated with the neutrals are excluded and the neutral temperature is set equal to the ion temperature.

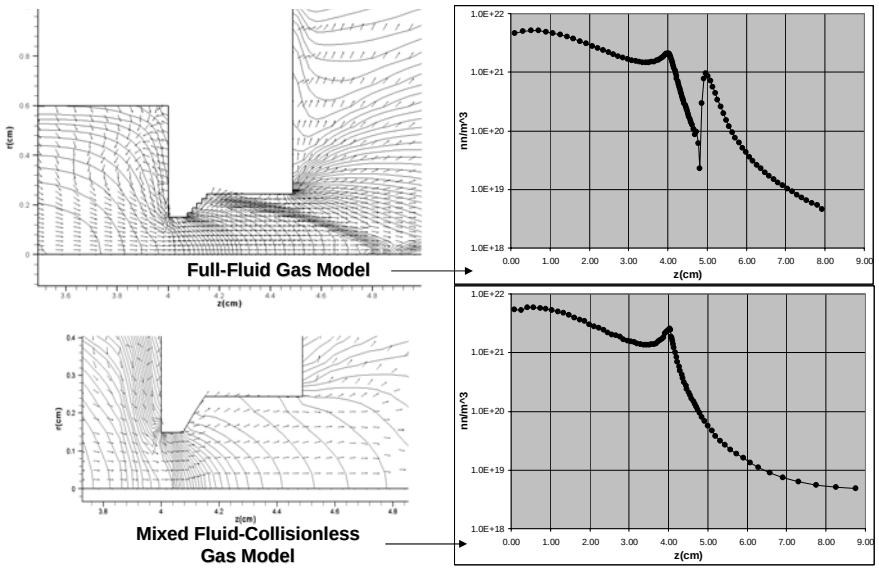

Fig 5. Comparison of the neutral gas density solution between the original fluid approach and the new fluid-collisionless approach.

FIG? (Left) below compares density contours overlaid by (unit) neutral gas velocity vectors between the old full-fluid model approach and the new mixed full fluid-full collisionless approach. The centerline plots of the neutral gas density (right) show how the new approach eliminates the shock predicted by the fluid solution but retains all the real features such as the enhanced density at the orifice entrance. The latter is a consequence of the neutral flux emanating from the orifice plate surface as a result of neutralized ions which is accounted for in OrCa2D-II.

III. Results and Comparisons with Measurements

A. Measurements

Measurements from two different hollow cathode tests performed at JPL are cited in this paper. Both tests used the same cathode operating at very similar conditions but utilized different anode configurations. The first test was conducted in 2004 and used a segmented anode[3] (FIG? left) and the second test, conducted this year, employed a planar anode (FIG? right).[4] The main purpose for the planar anode test was to obtain measurements in the exact same setup that OrCa2D-II simulates. The measurements used here for the comparisons were obtained without an applied magnetic field since OrCa2D-II does not yet account for the Hall effect. The test setup and diagnostics are described in detail in Ref. 4. FIGS? And FIG? show the

Fig 6. Left: Segmented anode test. Right: Planar anode test.

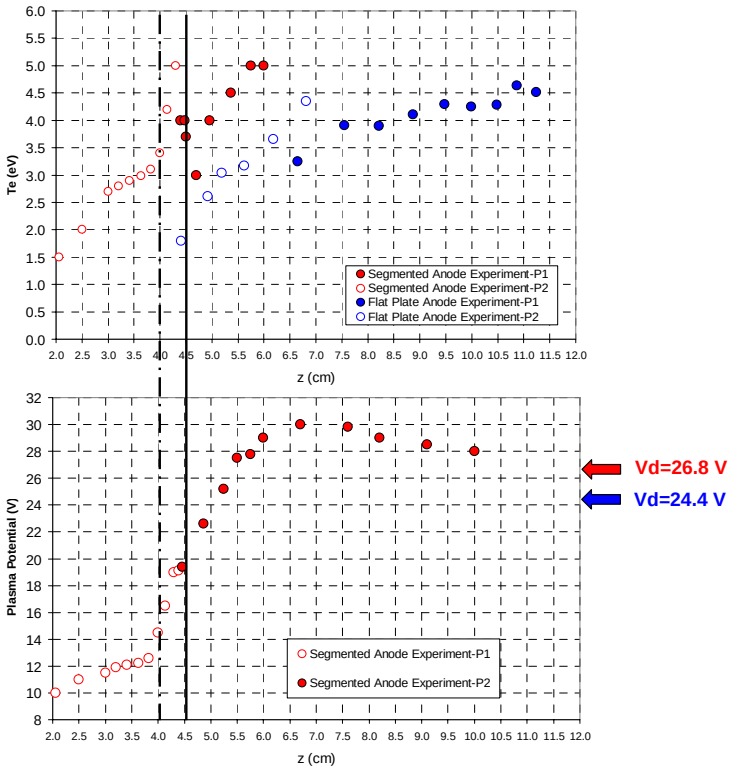

Figure 7. Electron temperature and plasma potential measurements taken during the segmented and planar anode tests. Segmented anode operating conditions: Id=25 A, mass flow rate = 5.5 sccm, Vd=26.8 V, B=0 T. Planar anode operating conditions: Id=27.5 A, mass flow rate = 5.5 sccm, Vd=24.4 V, B=0 T. The solid line indicates the location of the keeper exit. The dash-dotted line indicates the location of the orifice entrance. Experimental errors: Te =+/- 0.5 eV, ϕ=+/- 1eV.

B. Simulations

Earlier work with the rectilinear-grid version of OrCa2D-II postulated the existence of anomalously enhanced resistivity to explain the elevated electron temperatures observed in the orifice and plume regions. Specifically, simulations with classical transport coefficients predicted a much steeper fall of the plasma density in the plume region compared to the measurement (see FIG? black line). The computed electron temperatures and plasma potentials were also very low, in the order of 2 eV and 11 V, respectively (FIG? black line). Much of our efforts to understand the discrepancy have been driven by the Generalized Ohm's law which, after neglecting the ion contribution for simplicity, may be written as:

$$\nabla\phi \approx -\eta \mathbf{j}_e + \frac{\nabla(nT_e)}{n} \qquad (2)$$

If the plasma obeys EQN? then the steep rise of the plasma potential can only be due to two competing forces: the resistive electric field (drives the potential slope more positive) and the pressure gradient force (drives the potential slope less positive). Several improvements in the model physics have been incorporated this year all of which, ideally, either lead to an increase of the magnitude of the resistive term in EQN? or a decrease of the magnitude of the pressure gradient term. The impact of these effects is quantified in this section.

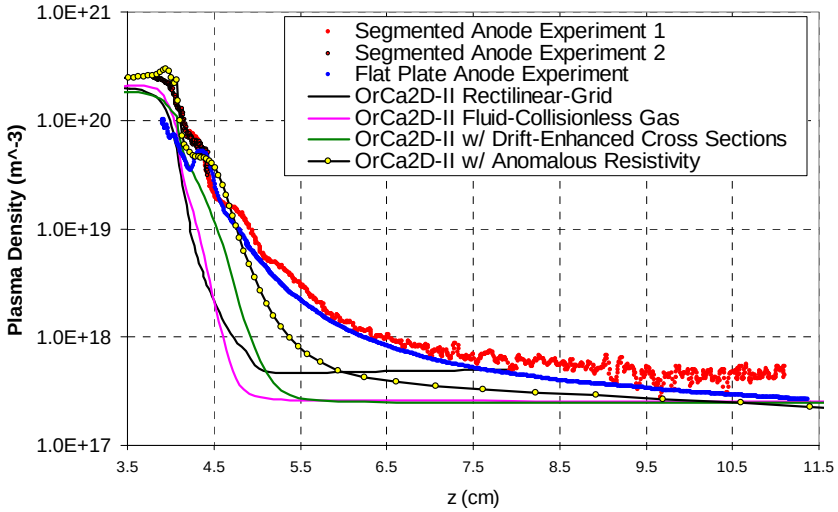

Fig 8. Comparisons between measured and calculated plasma density along the hollow cathode centerline.

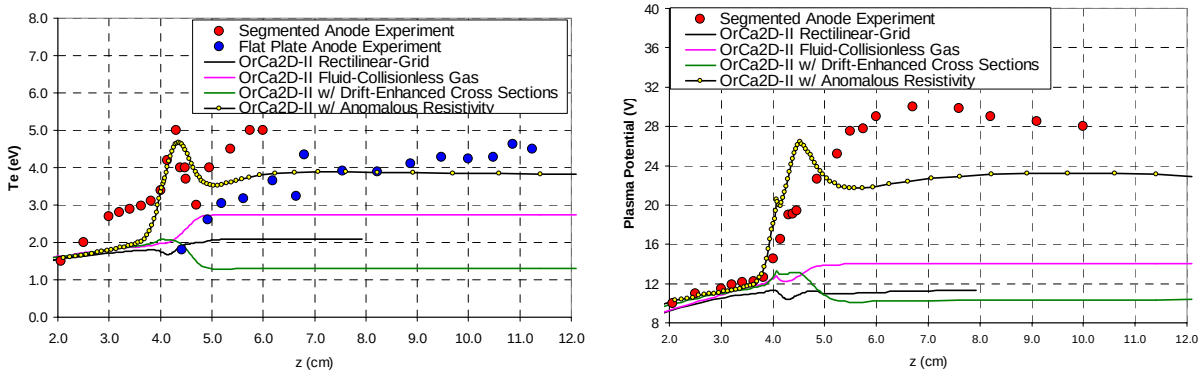

Fig 9. Comparisons between measured and calculated electron temperature (left) and plasma potential (right) along the hollow cathode centerline.

1. Effects of collisionless neutral gas

The mixed fluid-collisionless model for the neutral gas described in a previous section naturally leads to increased neutral gas densities in the orifice and keeper regions since regions of rarefaction behind shocks have been eliminated. Emission of neutral particles from warm boundaries also contributes to the enhancement of the neutral gas density inside these regions. FIG? shows that for the same plasma background the collisionless neutral gas density can be as many as 4x higher that predicted by the fluid model by the time it reaches the keeper exit. For fixed plasma conditions an increased in the neutral gas density will lead to increases in the ionization rate. When the plasma is allowed to evolve simultaneously with the neutral gas however, it is found that only modest increases in the plasma density are achieved (about a factor 2) while the downstream fall of the plasma density remains very steep as shown in FIG?.

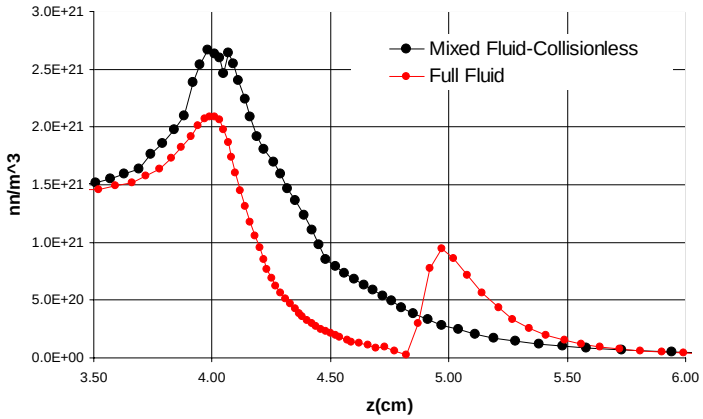

Fig 10. Comparison of the neutral gas density along the centerline as computed by the full-fluid and mixed fluid-collisionless model.

2. *Effects of classically-enhanced collision cross sections by the electron drift*
Previous work also showed that the electron Mach number defined as:

$$M_e \equiv \frac{|\mathbf{j}_e|}{en\sqrt{2eT_e/m_e}} \tag{3}$$

greatly exceeded unity in the near plume region. At high electron drifts a drifting Maxwellian distribution function must be implemented in the determination of the collision cross sections which can greatly enhance the cross section. For the xenon ionization cross section for example M_e=1 lowers the effective ionization potential by 40% which reduces $\exp(-\varepsilon_i/T_e)$ by more than 50x. Defining the following parameters,

$$\begin{aligned} &v \equiv \left(v_1^2+v_2^2+v_3^2\right)^{1/2},\ v_{rel} \equiv v + v_{drift},\ \varepsilon_{rel} = \tfrac{1}{2}m_e\left[v_1^2+v_2^2+(v_3+v_d)^2\right] \\ &\rightarrow f(v_1,v_2,v_3) = \exp\left(-\frac{\frac{1}{2}m_e v^2}{T_e}\right) \equiv \exp(-M^2), \end{aligned} \tag{4}$$

then the following non-dimensional quantities

$$\varepsilon_{rel}/T_e = M_1^2+M_2^2+(M_3+M_d)^2,\ M_{rel} = M_1^2+M_2^2+(M_3+M_d)^2 \tag{5}$$

may be used to yield,

$$\langle v\,\sigma\rangle = \bar{c}_e\ \frac{\iiint \exp(-M^2)\,M_{rel}\,\sigma(\varepsilon_{rel})\,dM_x dM_y dM_z}{\iiint \exp(-M^2)\ M\,dM_x dM_y dM_z} \equiv \bar{c}_e\ \langle\sigma\rangle,\ \bar{c}_e = \left(\frac{8eT_e}{\pi m_e}\right)^{1/2} \tag{6}$$

for the drift-enhanced collision cross section. Polynomial fits to the integral above for the e-n and ionization collision cross sections are shown in FIG?. It is noted that at T_e=2 eV for example a drift of M_e=2 implies an enhancement of 3.5× and more than 100× for the e-n and ionization cross-sections, respectively.

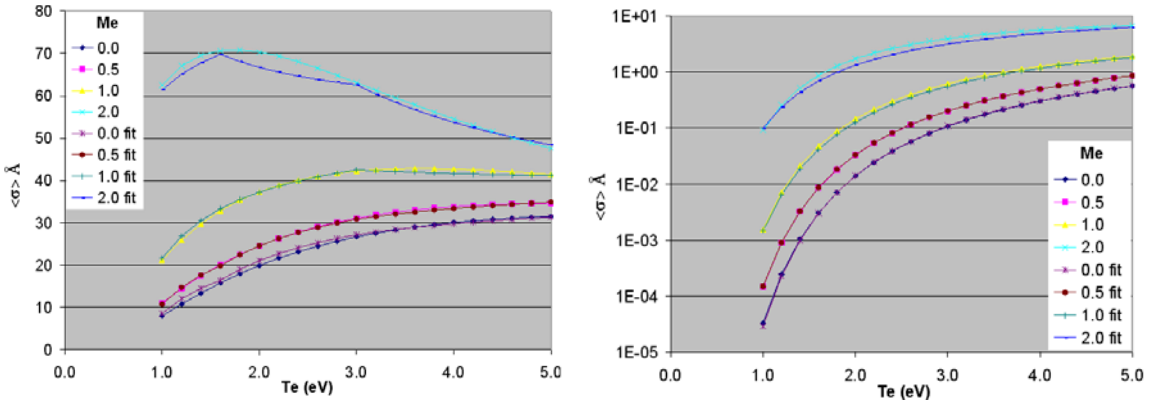

Fig 11. Drfit enhanced collsion cross sections and numerical fits. Left: e-n. right: ionization.

Results form numerical simulations that incorporated the drift-enhanced cross-sections are compared with the zero-drift results in FIG?. The 2-D density profiles show a 5× increase in the plasma density near the keeper exit and a similar drop in the electron drift Mach number. The orders of magnitude change implied by FIG? above is not attained because the electron temperature has also dropped upon employment of drift-enhanced cross sections as shown in FIG? For example at approximately z=5cm $n=2.8\times10^{17}$ m^{-3}, T_e=2.7 eV which gives ν_{ei}=2.1MHz and ν_{en}=31.3MHz for the case of no drift effects. By comparison, at the same location M_e=1.2 and $n=6\times10^{17}$ m^{-3} but T_e=1.3 eV which gives ν_{ei}=11.6 MHz and ν_{en}=10.5 MHz, thus the plasma resistivity is in fact lower at this location. It is found that because the enhancements of the classical e-n collision cross-section by the drift are only modest compared to ionization cross section (FIG?), the enhanced resistive heating ηje2 is not sufficient to account for the electron energy losses $en\nu_{iz}\varepsilon_i$ associated with the enhanced ionization and thus the electron temperature is reduced. The latter further supports the hypothesis that non-classical enhancements of the plasma resistivity are needed to explain the observed elevated temperatures.

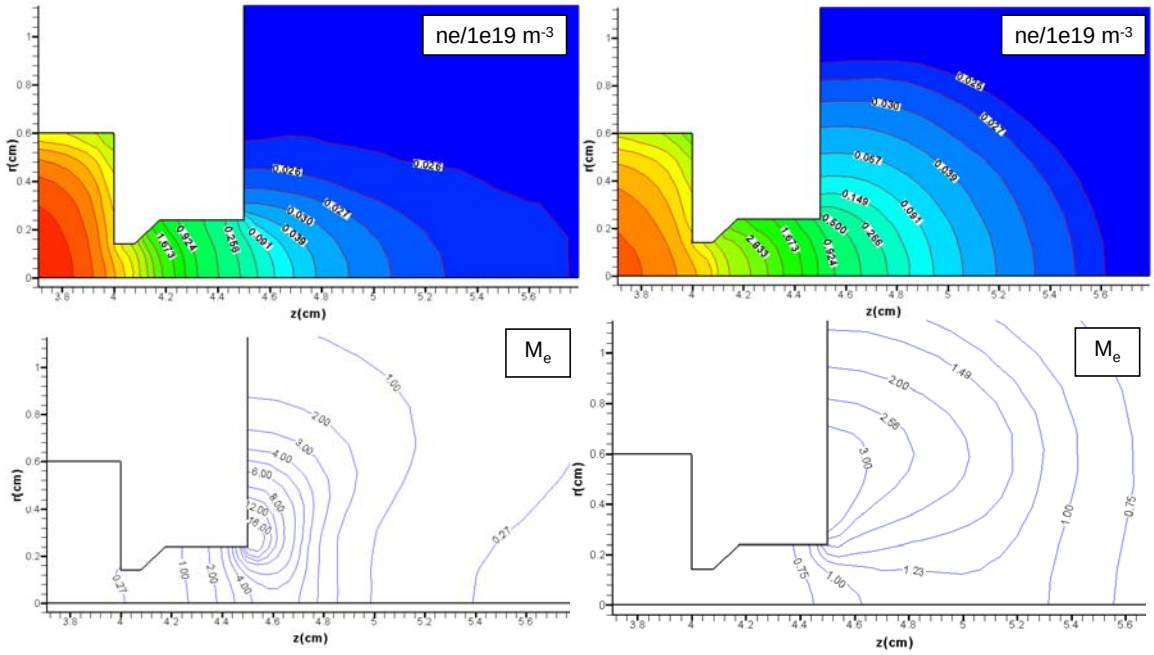

Fig 12. Comparison of the plasma density and Me in the keeper region for the cases of with and without drift enhancement of the collision cross sections.

3. Effects of anomalous resistivity

Since the beginning of the hollow cathode modeling work the possibility of enhanced resistance resulting from two-streaming instabilities has been proposed as the likely mechanism that leads to the highly elevated electron temperatures and steep plasma potential gradients measured in the proximity of the keeper orifice. The hypothesis is partially based on the high e-i relative drifts calculated by OrCa2D in the near-plume region. Anomalous mechanisms and loss of collisionality between electrons in the plume region can lead to deviations from the Maxwellian electron energy distribution function (EEDF) and to "runaway" electrons, which would also support the presence of "primary" electrons in the discharge chamber of the ion engine. If the deviations from the Maxwellian EEDF are not large then there it may be possible to model the electron-wave effects by proper forms of the resistivity.

Previous work has briefly looked at ion-acoustic and Buneman instabilities. The current-driven ion acoustic waves become unstable when the relative e-i drift velocity exceeds the ion acoustic speed $C_s \equiv [2e(T_e+T_i)/m_i]^{1/2}$ but is less than the electron thermal speed, $u_{T,e} \equiv (2eT_e/m_e)^{1/2}$. The instability also requires that $T_e >> T_i$. R.A. Treuman proposes that the well-known Sagdeev ion-acoustic anomalous collision frequency:

$$\nu_A^s \approx 10^{-2} \frac{T_e}{T_i} \frac{u_d}{C_s} \omega_{pi} \tag{7}$$

applies under the condition $M_i = u_d/C_s < 6$ to avoid Landau damping of the waves.[5] Beyond that Treuman proposes that third order terms come into play, which reduces the collision frequency with the third power of the drift velocity. Our previous work with EQN? implemented the full anomalous frequency without limit which led to exceedingly high resistivity in the far plume regions. We impose Treuman's limit in this work.

The plasma is subject to the to the electron-ion two-stream Buneman instability if $M_e = u_d/u_{T,e} > 1$. It is noted that for xenon, $M_i = 6$ implies $M_e = 0.012$ (when Te>>Ti) so the ion acoustic instability can be excited at much lower electron drifts when the condition on Te/Ti is satisfied. When $M_e > 1$ the anomalous resistivity is expressed by:

$$\nu_A^B \approx \alpha \omega_{pe} \left(\frac{m_e}{m_i} \right)^{1/3} \tag{8}$$

with coefficients α reprted to vary in the literature from 0.2 to 0.5. Various authors have also proposed different exponents for the mass ratio, namely 0.5[5] and 2/3.[6] No work has yet been conducted to quantify the anomalous mechanisms in the intermediate regions of M_e. Thus, for preliminary assessments we impose EQN? with $\alpha = 0.25$ for $Mi \geq 6$. The results for the electron temperature and plasma potential are shown in FIG? The distinguishing feature in these results compared to any obtained thus far is the closer agreement between these quantities in the plume region. Noted is the likely unphysical "bump" in T_e and ϕ which occurs inside the orifice region as a result of the hard condition imposed for "turning on" the anomalous resistivity. The effect is better illustrated in FIG? which plots the collision frequencies along the centerline. The discontinuous jump from classical to anomalous frequency is obvious at z~ cm where the condition on M_e is met. In reality, the transition from the relatively benign ion-acoustic instability to the more violent Buneman mode will likely be smoother. Work to identify the intermediate modes is ongoing. The comparison with the density (FIG?) continues to show a discrepancy which is likely due to the missing intermediate modes. Additional missing physics that may play a role in the evolution of the plasma downstream of the keeper are described next.

4. Missing physics

Self-induced magnetic field. The high current cathode studied here operates at a discharge current of 25-27.5 A which implies a self-induced (azimuthal) magnetic field of a little over 20 G at the keeper exit. Using the measured values for n and Te, and the computed value for n_n, the corresponding electron Hall parameter $\Omega_e = e|B|/m_e(\nu_{ei}+\nu_{en})$ is about 2 which implies a potential pinching effect by the magnetic field. The highest hall parameter is expected along the keeper where the maximum magnetic field is highest, dropping as ~1/r, and the collision cross sections is lowest dropping faster than 1/r. A high Hall parameter however does not necessarily imply significant confinement by the field if the electrons are not magnetized. FIG? below lists both the Hall and magnetization parameter defined as

$$\mu \equiv r_{L,e} \frac{|\nabla B|}{B} \tag{9}$$

where $r_{L,e}$ is the electron Larmor radius (using the electron thermal speed) and the second RHS term denotes the characteristic length associated with the variation of the self-induced magnetic field. The values in the last column imply that the magnetization parameter is in the order of unity, which imply finite-Larmor radius effects. The high Hall parameters also imply the possibility of some confinement by the self-induced magnetic field despite the estimates on the Larmor radius.

Table I. Radial values determining the electron Hall and magnetization parameters at z=4.8 cm ("m" denotes measured value, "c" denotes value determined by numerical simulation)

r(cm)	T_e (eV)^m	n (m^{-3})^m	B (T)^c	nn (m^{-3})^c	Ω_e	μ_e
1.14	4.16	1.40E+18	3.90E-04	4.00E+18	1.08E+01	8.91E-01
0.94	2.94	1.70E+18	4.50E-04	4.50E+18	7.10E+00	6.18E-01
0.70	2.39	2.45E+18	5.30E-04	5.00E+18	4.65E+00	3.07E-01
0.42	2.45	3.25E+18	6.00E-04	1.60E+19	3.90E+00	4.23E-01

Electron inertia. It is well known that when the electron drift approaches the thermal speed the possibility for the excitement of instabilities exists. Under such conditions the applicability of Generalized Ohm's Law is in question for two main reasons. First, if the instability leads to major deviations from the Maxwellian EEDF then the fluid approximation (inherent in Ohm's Law) fails and anomalous resistivity models are insufficient. A second reason may exist even in the case of small deviations from the Maxwellian and is best illustrated by writing the electron steady-state momentum equation as follows:

$$nm_e(\mathbf{u}_e \cdot \nabla)\mathbf{u}_e \approx -ne\mathbf{E} - \nabla p_e - nm_e(\nu_{ei} + \nu_{en})\mathbf{u}_e, \qquad (\mathbf{u}_e >> \mathbf{u}_i, \mathbf{u}_e >> \mathbf{u}_n) \tag{1}$$

EQN? above assumes no ionization and neglects the ion current. The derivation of Generalized Ohm's Law proceeds from this point on to eliminate the LHS term, namely the electron inertia. In all our calculations thus far, which employ the (inertia-less) Generalized Ohm's Law, it has been shown how the pressure-gradient term dominates the evolution of the plasma properties in the plume region. We can assess the importance of the electron inertia term as follows against the pressure gradient by defining the following ratio while neglecting the temperature-gradient:

$$\beta \equiv \frac{m_e n u_e \nabla u_e}{\nabla p_e} = \frac{m_e n u_e \nabla u_e}{eT_e \nabla n + n \nabla eT_e} \approx \frac{u_e^{\,2}}{eT_e / m_e} \frac{|\nabla u_e| / u_e}{|\nabla n| / n} \equiv 2M_e^{\,2} \left| \frac{\ell_u}{\ell_n} \right| \tag{2}$$

In EQN? above quantities ℓ_u and ℓ_n are characteristics lengths associated with spatial changes in the electron velocity field and density field respectively. The ratio of the lengths will be in the order of unity as determined by the electron continuity equation so for M_e in the order of unity the opportunity for the electron inertia term to play an important role exists even in the case of a stable electron fluid. No such effects have been included in our calculations thus far.

Acknowledgments

The research described in this paper was carried out by the Jet Propulsion Laboratory, California Institute of Technology, under a contract with the National Aeronautics and Space Administration.

References

[1] I. Mikellides, I. Katz, D. Goebel and J. Polk, *J. Appl. Phys*, **98**, (2005).
[2] I. Mikellides, I. Katz, D. Goebel, J. Polk and K. Jameson, *Physics of Plasmas*, to appear in the June 2006 issue.
[3] D.M. Goebel, A. Sengupta, A. Watkins, K. Jameson, AIAA Paper 04-3430, 40th AIAA/ASME/SAE/ASEE Joint Propulsion Conference, Fort Lauderdale, Florida, 2004.
[4] K. Jameson, D. Goebel and R. Watkins, AIAA Paper 06-4490, 42nd AIAA/ASME/SAE/ASEE Joint Propulsion Conference, Sacramento, California, 2006.
[5] R. Treumann, *Earth Planet Space*, **53**, pp. 453-462 (2001).
[6] A. Hirose, *Plasma Physics*, 20, pp. 481-485, (1978).